

# Nanostructured Boron-Doped Ultra-nanocrystalline Diamond Micro-pyramids: Efficient Electrochemical Supercapacitors

*Shradha Suman, Dhananjay Kumar Sharma, Ondrej Szabo, Benadict Rakesh, Marian Marton, Marian Vojs, Kamatchi Jothiramalingam Sankaran,\* and Alexander Kromka\**

*Shradha Suman, Benadict Rakesh, Kamatchi Jothiramalingam Sankaran*

*CSIR-Institute of Minerals and Materials Technology, Bhubaneswar 751013, India.*

*Academy of Scientific and Innovative Research (AcSIR), Ghaziabad 201002, India.*

*E-mail: [kjsankaran@immt.res.in](mailto:kjsankaran@immt.res.in)*

*Dhananjay Kumar Sharma, Ondrej Szabo, Alexander Kromka*

*Institute of Physics of the Czech Academy of Sciences, 16200 Prague, Czech Republic.*

*E-mail: [kromka@fzu.cz](mailto:kromka@fzu.cz)*

*Marian Marton, Marian Vojs*

*Institute of Electronics and Photonics, Slovak University of Technology, 81219 Bratislava, Slovakia.*

---

## ABSTRACT

The miniaturization of electrochemical supercapacitors (EC-SCs) requires electrode materials that are both durable and efficient. Boron-doped diamond (BDD) films are an ideal choice for EC-SC due to their durability and exceptional electrochemical performance. In this study, nanostructured boron-doped ultra-nanocrystalline diamonds (NBUNCD) were fabricated on Si micro-pyramids (Si<sub>p</sub>) using a simple reactive ion etching (RIE) process. The high aspect ratio and the induction of  $sp^2$  graphite in these nanorod electrodes during the etching process achieved a maximum specific capacitance of 53.7 mF cm<sup>-2</sup> at a current density of 2.54 mA cm<sup>-2</sup>

<sup>2</sup>, with a 95.5% retention after 5000 cycles. Additionally, the energy density reached 54.06  $\mu\text{Wh cm}^{-2}$  at a power density of 0.25  $\mu\text{W cm}^{-2}$ . A symmetric pouch cell using NBUNCD/SiP exhibited a specific capacitance of 0.23  $\text{mF cm}^{-2}$  at 20  $\mu\text{A cm}^{-2}$ , an energy density of 31.98  $\mu\text{Wh cm}^{-2}$ , and a power density of 0.91  $\mu\text{W cm}^{-2}$ . These superior EC properties highlight NBUNCD/SiP's potential for advancing miniaturized supercapacitors with high capacitance retention, cycle stability, and energy density.

---

**Keywords:** ultra-nanocrystalline diamond, nanorods, boron, supercapacitors, micro-pyramids, graphite

## 1. INTRODUCTION

In the generation of relentless pursuit of innovation, miniaturized devices stand poised on the pillars of efficiency, durability, and safety in energy storage. Intense research has been conducted to address the limitations in power densities and the lifetime of current rechargeable batteries, which aligns with ongoing global efforts.<sup>[1]</sup> Traditionally, batteries harness high energy density via a slow reversible electrochemical reaction. In contrast, EC-SCs store energy at the electrode-electrolyte interface through electrostatic adsorption/desorption and/or a fast Faradaic mechanism. This allows them to deliver a high amount of energy in a comparatively short duration of time, i.e., high power density, along with faster charging and discharging rates and significant lifecycle stability.<sup>[2]</sup> The unique capability of the EC-SCs to near-instantaneous power discharge renders them ideal for applications requiring uninterrupted power delivery. Notably, the EC-SCs are currently well-suited for devices requiring short bursts of high power, as is preferred in hybrid automobiles such as buses, trains, elevators, and cranes for regenerative braking and burst mode power delivery. Furthermore, the EC-SCs are extensively utilized in the realm of medical equipment, as well as short-term energy storage devices.<sup>[3]</sup>

The demand for energy storage systems has redirected attention towards finding solutions to the drawbacks of both batteries (slow rates and low power density) and SCs (relatively low energy density). The remedy to this problem is found by exploring and exploiting electrode materials.<sup>[4,5]</sup> The energy density of the SC can be enhanced by improving the specific capacitance ( $C_s$ ) and/or the operating voltage ( $V$ ) of the system (as  $E = 1/2 CV^2$ ).<sup>[1]</sup> To enhance the  $C_s$ , various electrode materials such as transition metal oxides, carbon allotropes (graphene, CNTs, fullerenes, activated carbons), and their composite materials have been investigated to improve EC performance by increasing specific surface area, porosity, and conductivity.<sup>[3]</sup> The enhancement of working potential ( $V$ ) can be achieved through three routes: i) the use of organic electrolytes in symmetric SCs, ii) the design of asymmetric SCs, and iii) the selection of larger electrochemical potential window samples.<sup>[6,7]</sup> However, the second method has several inherent drawbacks, including decreased conductivity, reduced safety, and environmental unfriendliness. Therefore, the optimization of electrode material was chosen as a viable approach. However, the characteristics of high-performance SC electrodes are (i) high surface area (as the charge is stored at the surface of the electrode), (ii) electronic and ionic conductivity (provides efficient electron pathways for charge transport), and (iii) mechanical and chemical stability (as phase change and side reactions of the active materials are the major cause of cycle instability).<sup>[8]</sup>

Diamond, the known hardest, chemically inert, anti-fouling and corrosion-resistant material, can be employed for the electrode materials in EC-SC to overcome stability issues. The diamond samples with a high defect density are stable in harsh environments, such as acidic electrolytes and higher operating temperatures.<sup>[5]</sup> Yet, they exhibit a rich surface chemistry, indicating that diamond electrodes can be used to develop novel types of SCs.<sup>[9]</sup> Other carbon-based electrode materials in a redox-active electrolyte, such as carbon nanotubes, show 5-9  $\mu\text{F cm}^{-2}$  specific capacitance,<sup>[10]</sup> and graphene shows 10-40  $\mu\text{F cm}^{-2}$ ,<sup>[11]</sup> whereas BDD shows 234

- 300  $\mu\text{F cm}^{-2}$ .<sup>[12,13]</sup> The BDD film is a promising electrode in the EC-SC because it possesses a wide electrochemical working potential in all types of electrolytes, along with high mechanical hardness, chemical inertness, and thermal stability. However, the bulky BDD film has large micron-sized grains, resulting in low capacitance values and high interfacial impedance, limiting its performance as EC electrodes.<sup>[14,15]</sup> Therefore, several attempts have been made to reduce the grain sizes of diamonds, and boron-doped ultra-nanocrystalline diamond (BUNCD) has been fabricated via chemical vapor deposition (CVD) methods with a diverse set of favorable properties, making BUNCD suitable for use in EC devices.<sup>[16,17]</sup> The BUNCD inherits all the robust qualities of diamonds but in smaller grain sizes, exceeding the physical and chemical properties of conventional diamonds.<sup>[18,19]</sup> The decrease in diamond grain sizes increases the number of grain boundaries, thereby enhancing the  $sp^2/sp^3$  ratio in the material along with the content of other forms of non-diamond carbon, such as amorphous carbon and hydrocarbons.<sup>[18]</sup> The BUNCD films possess remarkable chemical inertness and substantial stability, even at high current densities and potentials. Moreover, the BUNCD film has a wide potential window of approximately 3.2 V in aqueous and 4.6 V in organic solutions, making it an exceptional choice for EC applications.<sup>[20]</sup>

In order to further augment the EC-SC performance, efforts were directed towards amplifying the surface area. Two standard methods for achieving this are substrate structuring and the fabrication of diamond nanostructures. Before the diamond CVD, texturing the substrate enhances the electrical conductivity of thin films and provides a high aspect ratio template.<sup>[21]</sup> Over the past decades, researchers have successfully achieved substrate structuring through chemical vapor etching, laser ablation, lithography, RIE, and thermal evaporation/deposition techniques.<sup>[22–26]</sup> These methods have yielded substrates with nanowires, erect or inverted pyramids, and more. However, these approaches rely on sophisticated advanced equipment and complex processing steps, which makes them both time-

consuming and expensive. To overcome these limitations, the use of alkali wet-etching of substrates provides a relatively simple, efficient, and cost-effective approach for fabricating structured substrates.<sup>[21, 27, 28]</sup> Several etching methods for the diamond post-growth treatment have been reported as the second approach to enhancing surface area through diamond nanostructuring.<sup>[29]</sup> However, due to the extreme hardness of diamonds, wet etching is ineffective for structuring diamond films. RIE has become a particularly preferred method for creating nanostructures on diamond surfaces due to its convenience, cost-effectiveness, and significant improvement in areal densities and reproducibility.<sup>[30, 31]</sup>

This work describes the fabrication of NBUNCD over a Si<sub>P</sub> substrate. The Au mask-assisted RIE process is employed to create nanostructures on BUNCD films. The resulting NBUNCD on Si<sub>P</sub> was employed as an EC-SC electrode and exhibited a remarkable current response and high stability. The electrode was characterized using cyclic voltammetry (CV) and galvanostatic charging-discharging (GCD) techniques to examine the enhanced EC characteristics. Electrochemical impedance spectroscopy (EIS) was employed to study the effect of micro-pyramid structure on the substrate and nanostructuring of BUNCD on the EC performance of the electrode. Furthermore, this study estimates the specific capacitance, lifecycle stability, energy and power densities of the electrode, and power densities. The results show that the EC-SC performance of the NBUNCD/Si<sub>P</sub> electrode is enhanced compared to other nanostructured electrodes. This enhancement is attributed to the high aspect ratio and the presence of sp<sup>2</sup> graphite in the electrode.

## **2. RESULTS AND DISCUSSION**

The surface morphology FESEM micrographs of the Si<sub>P</sub> are shown in Figure 2a. The formation of micron-sized pyramids is distinctly visible in the 45° angle view FESEM micrograph in Figure 2a<sub>I</sub>. The micro-pyramids of various sizes are randomly distributed throughout the Si substrate. The width of the micro-pyramids calculated from Figure 2a<sub>II</sub> varies

from 0.5 to 10  $\mu\text{m}$ , and the height ranges between 0.4 to 5.5  $\mu\text{m}$ , calculated from cross-sectional FESEM Figure 2a<sub>III</sub>.

These structured Si-substrates were then subjected to the LA MW CVD reactor for the diamond deposition, resulting in a uniform coating of BUNCD over the Si<sub>P</sub> structures. The 45° angle view FESEM micrograph shown in Figure 2b<sub>I</sub> depicts a uniform coating of BUNCD over Si<sub>P</sub>. The grain sizes for the BUNCD/Si<sub>P</sub>, calculated from the top view FESEM micrograph Figure 2b<sub>II</sub>, range from 20–30 nm with a cauliflower shape.<sup>[25]</sup> Figure 2b<sub>II</sub> shows a smooth surface with many agglomerated grains, as previously observed for undoped UNCD films grown in Ar-rich plasma.<sup>[32–34]</sup> The cross-sectional FESEM micrograph analysis from Figure 2b<sub>III</sub> reveals that the deposition thickness of the BUNCD film is approximately 4  $\mu\text{m}$ .

The nanostructure fabrication commenced by evaporating an Au-layer of 8 nm thickness over the BUNCD/Si<sub>P</sub> film, followed by annealing in microwave plasma at 500 °C, which resulted in self-organized nano-droplets of Au on the BUNCD/Si<sub>P</sub> film. Figure S1 shows the top-view FESEM micrograph of Au nano-droplets on BUNCD/Si<sub>P</sub>, which were used as the mask; their diameter ranges from 40–65 nm.<sup>[35]</sup> However, clusters of seemingly smaller Au nano-droplets with diameters ranging from 10–20 nm can also be identified. Due to the structured character of the BUNCD/Si<sub>P</sub> surface, the smaller Au nano-droplets are preferentially formed at the foot valleys of the micro-pyramids. Subsequently, the Au/BUNCD/Si<sub>P</sub> film was subjected to RIE in O<sub>2</sub>/CF<sub>4</sub> plasma. The Au nano-mask-covered area remained unchanged, whereas the remaining diamond surface was etched out, resulting in vertically aligned nanorods standing upright over the BUNCD/Si<sub>P</sub> film. Figure 2c<sub>I</sub> shows the 45° angle view FESEM micrograph of NBUNCD/Si<sub>P</sub> where a large number of nanorods are distinctly visible with a wide range of tip-diameter up to 65 nm, as calculated from Figure 2c<sub>II</sub>. The length of the nanorods is approximately 220 nm, and the width is around 40–60 nm, as calculated from Figure 2c<sub>III</sub>. Nano-whiskers with smaller tip diameters of around 10–20 nm were also observed

among the NBUNCD/Si<sub>P</sub> nanorod arrays. The formation of nano-whiskers can be attributed to two aspects. First, the diameter of the BUNCD grains is smaller than that of the diameter of the Au-mask, resulting in the formation of smaller Au nano-droplets at the valley of the micro-pyramids, along with an uneven etching of the diamond grains.<sup>[35, 36]</sup> Another reason can be the rapid anisotropic nature of RIE. The high-energy oxygen and fluorine ions in the plasma accelerate toward the diamond film under the influence of RF bias, as shown in Figure 3.<sup>[33, 34]</sup> This disrupts the BUNCD, and some of the carbon interacts with the plasma species, thus enhancing the efficiency of the etching process. The disordered carbon, such as hydrocarbons and/or amorphous carbons, at the grain boundaries gets etched out due to the highly energetic oxygen ions resulting in nano-whiskers.<sup>[27, 28]</sup> The chemical reaction involved in the etching of diamond in the RIE system can be realized via the equation:  $C_{(diamond)} + CF_4 + O_2 \rightarrow C_{(accumulated)} + CF_x + CO$ , where  $C_{(diamond)}$  is carbon element of etched diamond and  $C_{(accumulated)}$  is the deposition of amorphous carbon over the diamond surface.<sup>[39]</sup> Figure 3 depicts the etching of the unmasked portion of BUNCD/Si<sub>P</sub> due to the bombardment of highly energetic ions on the diamond surface with an accumulation of carbon and emission of CO. Thus, the conversion of  $sp^3$ -bonded carbon to  $sp^2$ -bonded carbon occurs with the formation of BUNCD nanostructures.<sup>[40]</sup> However, due to the presence of Au-masks and CF<sub>4</sub>, the resulting nanostructures have nearly uniform lengths with smooth surfaces.<sup>[41]</sup>

For comparison, BUNCD films were also grown on a polished Si substrate, and the FESEM micrograph of BUNCD/Si is shown in Figure S2. The 45° angle view FESEM micrograph in Figure S2a depicts almost identical grains as BUNCD/Si<sub>P</sub>. The top view FESEM micrograph (Figure S2b) shows a smooth surface with 25–40 nm grain sizes. The cross-sectional FESEM micrograph in Figure S2c shows the thickness of the deposited film to be around 6.4 μm. The increase in surface area for BUNCD/Si<sub>P</sub> can be distinctly recognized by comparing the FESEM micrographs shown for BUNCD/Si and BUNCD/Si<sub>P</sub> in Figure S2 and Figure 2b, respectively.

The XRD spectrum of BUNCD/Si shown in Figure S3 reveals three distinct peaks at 43.9°, 75.2°, and 91.3°, corresponding to the (111), (220), and (311) planes of polycrystalline diamond, respectively. These peaks confirm the presence of the diamond phase.<sup>[42, 43]</sup>

The micro-Raman spectrum of the NBUNCD/Si<sub>p</sub> sample shown in Figure 4a is deconvoluted with the Guass function multiple peaks fitting in Origin software after subtracting the background line. The sample showed a distinct, characteristic diamond peak around 1280 cm<sup>-1</sup>.<sup>[44]</sup> The shift in the diamond peak is due to the interference between the zone-center phonon and the continuum of electronic transitions of BUNCD occurring because of the Fano effect.<sup>[45]</sup> The presence of dopant and grain boundaries in BUNCD causes a significant shifting of the peak. A series of characteristics of Raman signature peaks for the BUNCD samples are observed for all three BUNCD samples plotted in Figure 4a. Two broad peaks around 470 cm<sup>-1</sup> (B1) and 1190 cm<sup>-1</sup> (B2) are observed, attributed to the boron incorporation into the BUNCD lattice. The B1 and B2 peaks correspond to the reported maxima of phonon density of states (PDoS) and are sensitive towards the boron concentration due to the Fano effect and phonon confinement.<sup>[46–48]</sup> With the incorporation of a high concentration of boron, the diamond peak (typically around 1332 cm<sup>-1</sup>) suffers a drastic decrease in intensity with a significant shift to the lower wavenumber, and the relative intensity of the B1 and B2 peaks increases.<sup>[48]</sup> The B1 peak is significant because it has a one-to-one relationship with the boron concentration in the sample. The wavenumber of the B1 peak fitted with a Lorentzian function is employed to calculate the approximate boron concentration  $n = 1.8 \times 10^{21}$  in NBUNCD/Si<sub>p</sub>.<sup>[40,44]</sup> An additional minute peak is observed around 1020 cm<sup>-1</sup> due to PDoS resulting from symmetry breaking in the BUNCD sample, denoted as PDoS<sub>1</sub>.<sup>[47]</sup> The disordered carbon in the *sp*<sup>3</sup> cluster gives rise to a peak around 1320 cm<sup>-1</sup>, which is the D-peak. The *sp*<sup>2</sup> carbon gives rise to the graphitization peak, G-peak, in the BUNCD samples, observed around 1520 cm<sup>-1</sup>.



To understand the chemical bonding and elemental content in the BUNCD samples, XPS spectroscopy was employed. The C1s and O1s core level spectra fitted by the Lorentz function with the Shirley method of background correction for the BUNCD samples are shown in Figure 4b and c, respectively. The thin film samples, BUNCD/Si and BUNCD/Si<sub>P</sub> (spectra I and II of Figure 4b and c) showed very similar spectra. The *sp*<sup>3</sup>-carbon peak was observed at 284.2 eV for the thin film sample, whereas the nanostructured sample was at 285.2 eV (spectrum III of Figure 4b). The shift in the *sp*<sup>3</sup>-carbon peak is due to the destruction and reconstruction of the grain boundaries after the rapid etching via the RIE process.<sup>[49]</sup> In the case of NBUNCD/Si<sub>P</sub>, the presence of a OH-C=O peak at 288.9 eV arises due to the oxidation of the diamond during the nanostructuring process.<sup>[50]</sup> The presence of *sp*<sup>2</sup>-carbon in the thin film samples is also distinctly visible at around 283.8 eV. However, the nanostructured film possesses a slightly shifted C=C peak at 284.4 eV due to RIE. Data regarding the contents of elements in the sample calculated from the XPS spectra is shown in Table S1. The *sp*<sup>2</sup> content is higher for the case of NBUNCD/Si<sub>P</sub> due to the anisotropic rapid etching via RIE.<sup>[44]</sup> The presence of doped boron in the nanostructured sample appears to decrease, as seen in Figure 4b and the deconvoluted B1s spectra in Figure S4. The concentration of boron is expected to be lower in the case of NBUNCD/Si<sub>P</sub> due to the re-sputtering of the undoped amorphous carbon resulting from the RIE.<sup>[51]</sup> Figure 4c displays the O1s spectra of BUNCD samples, where three distinct peaks are observed, namely, O=C, B (531.5 eV), O-C, B, N (532.8 eV) and H<sub>2</sub>O (534.2 eV). As can be observed from Table S1, the O=C concentration for the BUNCD sample(s) nanostructured by O<sub>2</sub>/CF<sub>4</sub> RIE is higher than that for the non-etched thin film sample.

Atomic force microscopy (AFM) measurements were employed to assess the root mean square (rms) roughness of the BUNCD samples. The 8×8 μm<sup>2</sup> AFM scan is presented in Figure S5. The BUNCD/Si sample exhibited an rms roughness of 28.44 nm, attributed to the deposition of faceted grains on the planar Si substrate. In contrast, BUNCD/Si<sub>P</sub> showed an

increased roughness of 353.44 nm, resulting from the presence of micro-pyramids alongside the faceted grains. However, for NBUNCD/Si<sub>P</sub>, accurate roughness measurement was challenging due to the wider AFM tip relative to the spacing between the nanorods. Although a value of 398.03 nm was recorded, the actual roughness is likely higher.<sup>[52]</sup>

In order to study the EC performance of the BUNCD electrodes, cyclic voltammetry studies were carried out in the three-electrode cell setup configuration. Figure 5a-c displays the CV curves of BUNCD/Si, BUNCD/Si<sub>P</sub>, and NBUNCD/Si<sub>P</sub>, respectively, in 1M Na<sub>2</sub>SO<sub>4</sub> aqueous electrolyte in the potential window from 0 to 1 V vs. Ag/AgCl. The scan rates for the CV analysis varied from 10 to 100 mV s<sup>-1</sup>, and it was observed that the current response for all the samples increases with an increase in scan rates. A significant enhancement in the current response is observed in Figure 5c for the case of NBUNCD/Si<sub>P</sub>. The comparison of the CV curve of all the BUNCD samples taken at 60 mV s<sup>-1</sup> scan rate is plotted in Figure 5d. Even though the current responses for the BUNCD/Si and BUNCD/Si<sub>P</sub> are almost comparable, still a slight enhancement of capacitive current is resolvable for the BUNCD/Si<sub>P</sub>, which can be attributed to the enhancement of the surface area of a micro-pyramidal structure. An enhancement of the area enclosed by the CV curve in the case of NBUNCD/Si<sub>P</sub> is identified, which is attributed to the nanostructuring of the BUNCD film, increasing the area of interaction and the reactions of oxygen species present in NBUNCD/Si<sub>P</sub> after RIE. The nanostructuring improves the number of charge transport sites by enhancing the aspect ratio of the NBUNCD/Si<sub>P</sub> sample. The FESEM micrograph of NBUNCD/Si<sub>P</sub> shown in Figure 2c displays available sites to adsorb and enhance the ion to transfer charge. Moreover, since the nano-whiskers consist of disordered carbon containing *sp*<sup>2</sup>-graphitic carbon, they contribute well to the ion transfer process, thus enhancing the capacitive current of NBUNCD/Si<sub>P</sub>.<sup>[53, 54]</sup> The specific areal capacitance at different scan rates for the BUNCD samples is calculated using the following equation:

$$C = \frac{1}{2} \frac{\int I(V)dV}{\Delta V \times \vartheta \times A} \quad (1)$$

where  $\int I(V)dV$  is the total area or current enclosed by the CV curve,  $\Delta V$  is the scanned potential window,  $\vartheta$  is the scan rate under consideration, and  $A$  is the geometrical area of the working electrode. A comparative study of the specific areal capacitance calculated for the BUNCD electrodes at varied scan rates with a constant potential window is shown in Figure S6. The enhancement of the geometrical surface area in the case of BUNCD/Si<sub>P</sub> enhances the specific areal capacitance compared to BUNCD/Si. Moreover, the NBUNCD/Si<sub>P</sub> sample shows the highest specific areal capacitance value of 0.318  $\mu\text{F cm}^{-2}$  at 10  $\text{mV s}^{-1}$ .

GCD measurements of the BUNCD samples were investigated via charging and discharging the electrodes in the predefined CV potential window at varied current densities. Figure 6a-c displays the GCD curves of BUNCD/Si, BUNCD/Si<sub>P</sub>, and NBUNCD/Si<sub>P</sub>, respectively, in 1M Na<sub>2</sub>SO<sub>4</sub> aqueous electrolyte in the potential window from 0 to 1 V vs. Ag/AgCl recorded at current densities varied from 3.56 to 12.73  $\mu\text{A cm}^{-2}$ . Almost symmetrical triangle-shaped curves are observed for the BUNCD/Si electrodes. Here, rapid charging and discharging are observed at higher ends of the current densities. The specific capacitance for the BUNCD electrodes can be calculated using equation (2), as below:

$$C = \frac{1}{2} \frac{I \times \Delta t}{\Delta V \times A} \quad (2)$$

where  $I$  is the current applied for GCD analysis,  $\Delta t$  is the time taken to discharge to the minimum potential,  $\Delta V$  is the scanned potential window, and  $A$  is the geometric area of the working electrode. The corresponding values of the specific capacitance calculated from the GCD curves of the BUNCD electrodes are plotted against the applied current densities and are shown in Figure S7. Here, the distinct enhanced feature of higher specific capacitance for BUNCD/Si<sub>P</sub> is visible, but the highest specific capacitance is found for NBUNCD/Si<sub>P</sub> of value 0.39  $\text{mF cm}^{-2}$  at 3.56  $\mu\text{A cm}^{-2}$  current density. Table S2 presents a comparison of the EC

parameters of NBUNCD/Si<sub>P</sub> with those of other reported nanostructured electrodes, highlighting a substantial improvement in performance over previously documented results. The NBUNCD/Si<sub>P</sub> inherits higher  $sp^2$  content along with higher geometrical surface area, thus exhibiting better EDLC behavior and easy electrolyte ion transport. Thus, NBUNCD/Si<sub>P</sub> is a suitable electrode for EDLC-type applications. Figure 6d depicts a comparative plot of EIS of the BUNCD electrodes fitted with an equivalent circuit in the frequency range 0.1 Hz to 20 kHz. The equivalent circuit parameters with their corresponding values calculated from the circuit fitting are listed in Table 1. The equivalent circuit consists of an equivalent series resistance ( $R_S$ ) connected in series with a network containing a charge-transfer resistance ( $R_{CT}$ ) and a constant phase element (CPE) in parallel with a double-layer capacitance ( $C_{DL}$ ). The NBUNCD/Si<sub>P</sub> electrode demonstrates a lower  $R_S$  and  $R_{CT}$  value owing to its larger specific surface area. The NBUNCD/Si<sub>P</sub> surface, consisting of nanorods and nano-whiskers, provides better charge-transfer kinetics.<sup>[55, 56, 30]</sup> The clear increment of capacitance from BUNCD/Si to NBUNCD/Si<sub>P</sub> is evident in Table 1. Moreover, the value of the constant  $n$  for BUNCD/Si shows a resistive nature supported by the Bode-Bode plot in Figure S8. The phase angle ( $\phi = -90^\circ$ , ideal capacitor) for BUNCD/Si is  $-43^\circ$  depicting its resistive nature, whereas for BUNCD/Si<sub>P</sub> and NBUNCD/Si<sub>P</sub>, the phase angle is  $-62^\circ$  and  $-77^\circ$ , respectively.<sup>[56, 30]</sup> The constant  $n$  for BUNCD/Si<sub>P</sub> and NBUNCD/Si<sub>P</sub> also increases towards 1, implying the capacitive behavior of the electrodes.<sup>[57]</sup> The comparison of the values of CPE for BUNCD/Si and BUNCD/Si<sub>P</sub> shows a huge enhancement from 6.9 to 15.1, which can be attributed to the formation of the micro-pyramidal structure. However, the overall performance of NBUNCD/Si<sub>P</sub> is in a relatively lower impedance range, and better capacitive behavior is observed.

The PC behavior of the BUNCD electrodes is studied by employing a redox active electrolyte in 0.05M  $[\text{Fe}(\text{CN})_6]^{3-/4-}$  contained in 1M  $\text{Na}_2\text{SO}_4$  with a potential window from -1 to 1.5 V vs. Ag/AgCl in a similar three-electrode cell set up. The characteristic oxidation and

reduction peaks appeared for all the BUNCD electrodes, as shown in Figure 7a–c. The CV measurements are carried out at varied scan rates ranging from 10 to 100 mV s<sup>-1</sup>. Here, the enhancement of the area under the curve is accompanied by the enhancement of anodic-cathodic peak separation ( $\Delta E_p$ ). Figure 7d shows the overlapped plot of CV response for all three BUNCD electrodes in redox active electrolytes at 60 mV s<sup>-1</sup>. Figure S9 displays the variation of peak separation with the scan rates, and it is observed that only the NBUNCD/Si<sub>P</sub> sample shows reversible behavior with less peak separation. In contrast, the BUNCD/Si and BUNCD/Si<sub>P</sub> show an irreversible nature with a higher separation of peaks.<sup>[58]</sup> The reversibility and better electron transfer kinetics observed for the case of NBUNCD/Si<sub>P</sub> are assigned to *sp*<sup>2</sup>-graphitic phases and the high aspect ratio in the sample due to the RIE process. Figure S10 displays the variation of the anodic and cathodic current of the BUNCD samples plotted against the square root of the scan rates calculated from the CV curves shown in Figure 7a–c. The linear fitting of the plots suggests the reactions in the system are diffusion-controlled in nature.<sup>[61]</sup> Furthermore, the specific areal capacitance of BUNCD film calculated from the CV curves of Figure 7a–c is shown in Figure S11. The maximum specific areal capacitance of 0.14 mA cm<sup>-2</sup> at 10 mV s<sup>-1</sup> is observed for the NBUNCD/Si<sub>P</sub>. However, it is worth noting that the BUNCD/Si<sub>P</sub> sample also shows a better specific capacitance in the redox-active electrolyte than the BUNCD/Si sample. This confirms that the formation of micro-pyramids enhances the electrochemical performance of the BUNCD sample.

The redox-active electrolyte was further utilized to study the charging-discharging behavior of the BUNCD electrodes by applying varied current density at the predefined cut-off potential window observed from the CV measurement shown in Figure 7. Figure 8a–c shows a non-linear curve for all the BUNCD electrodes with a plateau region, signifying the PC characteristics of the electrodes. This distinct feature of PC behavior is observed due to the rapid Faradaic reaction of [Fe(CN)<sub>6</sub>]<sup>3-/4-</sup> at the electrode-electrolyte interface. Here, the

BUNCD/Si thin film sample shows a higher charging time of 70 s at a comparatively higher current of  $4.58 \text{ mA cm}^{-2}$ , whereas the BUNCD/Si<sub>P</sub> and NBUNCD/Si<sub>P</sub> show 50 s and 66 s, respectively, at a current density of  $2.54 \text{ mA cm}^{-2}$ . At  $2.54 \text{ mA cm}^{-2}$ , the BUNCD/Si sample does not charge up to the desired potential. The discharge time for BUNCD/Si is 38 s, implying the non-reversibility nature of the electrode in the redox active electrolyte. However, for BUNCD/Si<sub>P</sub> and NBUNCD/Si<sub>P</sub>, the charging and discharging times are comparable, i.e., 50 s and 64 s, respectively, implying better PC behavior. The specific capacitance of the BUNCD electrode calculated using equation (2) employing the GCD curves shown in Figure 8a–c is shown in Figure S12a–c, respectively. For the NBUNCD/Si<sub>P</sub> sample, Figure S12c shows a maximum specific capacitance of  $53.7 \text{ mF cm}^{-2}$  at a current density of  $2.54 \text{ mA cm}^{-2}$  and the ratio of discharge time to charge time, i.e., the Coulombic efficiency ( $\eta\%$ ) vs. current densities for the NBUNCD/Si<sub>P</sub> sample shows a 95% efficiency.

Figure 9 shows the typical Nyquist plot for the BUNCD electrodes with the corresponding equivalent circuits fitted for the spectra in  $0.05\text{M Fe(CN)}_6^{3-/4-}$  contained in  $1\text{M Na}_2\text{SO}_4$ . Figure 9a<sub>I</sub> shows the EIS spectrum of BUNCD/Si with the corresponding Randles circuit containing the equivalent series resistance ( $R_s$ ), charge transfer resistance ( $R_{CT}$ ), diffusion resistance ( $W_1$ ) and double layer capacitance ( $C_{DL}$ ) as shown in Figure 9a<sub>II</sub>. For the Faradaic reaction taking place ( $O + e^- \rightleftharpoons R$ ), the charging of the electrode is occurring in parallel. Hence,  $R_{CT}$  and  $C_{DL}$  are connected in parallel. However, the rate of Faradaic reaction is controlled by the diffusion of ions to the electrode surface; hence, the circuit consists of a series connection of Warburg element ( $W_1$ ) and  $R_{CT}$ .<sup>[58, 59]</sup> Figure 9b<sub>I</sub> shows the EIS spectrum of BUNCD/Si<sub>P</sub> with a distinctive semicircle and the equivalent circuit similar to BUNCD/Si but consisting of a CPE in place of  $C_{DL}$ . The CPE is added to model the non-ideal capacitance behavior of the electrode arising due to the surface roughness, non-homogeneity, and surface porosity.<sup>[57]</sup> The formation of micro-pyramids in the substrate enhances the surface area and

roughness, resulting in a non-ideal capacitance in the case of BUNCD/Si<sub>P</sub>. The equivalent circuit is critical for the NBUNCD/Si<sub>P</sub>, as shown in Figure 9c<sub>II</sub>. The first part of the circuit consists of the R<sub>S</sub>, describing the solution resistance and the internal resistance of the electrode. The second part consists of resistance arising due to the rate of redox reactions at the electrode-electrolyte interface in parallel connection with CPE, characterizing the frequency dispersion due to the formation of nanostructures, diffusion of ions, and nature of the electrode.<sup>[60]</sup> The final part consists of an R<sub>CT</sub> and a C<sub>DL</sub> associated with the kinetics of the electrode-electrolyte interface. The W<sub>1</sub> depicts the diffusion of ions into the porous structure of the electrode.<sup>[60, 61]</sup> The NBUNCD/Si<sub>P</sub> shows higher capacitance and less R<sub>CT</sub>, as shown in Table 2.

The comparative study of the specific capacitance retention and Coulombic efficiency is carried out for all the samples in both the electrolytes, as shown in Figure 10. In Figure 10a, the lifecycle stability of the BUNCD samples is studied by consecutively charging and discharging the sample 5000 times in 1M Na<sub>2</sub>SO<sub>4</sub> aqueous electrolyte and plotting the retention of specific capacitance (ratio of final capacitance to the initial capacitance multiplied by 100) vs. cycle number. It is apparent that the NBUNCD/Si<sub>P</sub> has the maximum stability, and the retention is 95.49%. On the other hand, after 5,000 cycles, the retention of specific capacitance falls to 67.40% and 69.26% for the BUNCD/Si and BUNCD/Si<sub>P</sub>, respectively. The Ragone plot for the BUNCD sample shown in Figure S13 depicts the NBUNCD/Si<sub>P</sub> sample possessing a higher energy density of 54.06 μWh cm<sup>-2</sup> at a power density of 0.25 μW cm<sup>-2</sup>. Figure 10c depicts the Coulombic efficiency variation with respect to cycle number, and the minimum recorded efficiency for the BUNCD/Si<sub>P</sub> (80.35%) is lower compared to BUNCD/Si<sub>P</sub> (89.71%) and NBUNCD/Si<sub>P</sub> (92.53%). Similar to results in aqueous electrolytes, the NBUNCD/Si<sub>P</sub> is found to have the highest retention in the redox-active electrolyte (Figure 10b). In this case, the stability after 5000 cycles in 0.05M [Fe(CN)<sub>6</sub>]<sup>3-/4-</sup> contained in 1M Na<sub>2</sub>SO<sub>4</sub> is 90.01%, 93.31%, and 94.05% for BUNCD/Si, BUNCD/Si<sub>P</sub>, and NBUNCD/Si<sub>P</sub>, respectively. The Coulombic

efficiency (Figure 10d) exhibits a similar trend, with the lowest efficiency recorded at 89.01% for BUNCD/Si, followed by 94.39% for BUNCD/Si<sub>P</sub>, and reaching 95.62% for NBUNCD/Si<sub>P</sub>. The resistive nature of the BUNCD/Si electrode, as observed from the impedance spectroscopy, strongly agrees with the Coulombic efficiency observations.

A comparative analysis of microstructural and chemical structural modification of NBUNCD/Si<sub>P</sub> before and after 5000 cycles of charging and discharging is accomplished employing FESEM and Raman spectroscopy. Figure S14a-b depicts the top-view surface morphology of NBUNCD/Si<sub>P</sub> before and after the lifecycle stability test. Figure S14a displays the nanorods with fuller circular tips, with the length of the nano-whiskers almost comparable to that of nanorods. However, Figure S14b shows flattened tips of nanorods and suppressed nano-whiskers. To further augment the chemical structure of the sample, Raman spectra of NBUNCD/Si<sub>P</sub> before and after the lifecycle are compared and shown in Figure S14c. The characteristic diamond peaks similar to Figure 4a are observed before and after samples. The variation of intensity and shifting of the peak position implies the modification in the surface chemical structure of the material as a result of the lifecycles test. Analysis of the ratio of the intensity of the D ( $I_D$ ) peak to  $sp^3$  ( $I_{sp^3}$ ) peak and the ratio of the intensity of  $sp^2$  ( $I_{sp^2}$ ) to  $sp^3$  ( $I_{sp^3}$ ) highlights the situation better. The  $I_D/I_{sp^3}$  ratio for the before sample is 2.66, whereas the ratio for the after sample is 2.84. There is a slight enhancement in the intensity of the D peak for the after sample, depicting the accumulation of amorphous carbon in the after sample. Moreover, the calculated value of the  $I_{sp^2}/I_{sp^3}$  ratio for the after sample is 3.40, whereas for the before sample, it is 3.76. This shows the reduction of graphitic carbon content in the sample after the lifecycle measurement. These observations strongly agree with the previously reported literature.<sup>[62–65]</sup> In diamond-graphitic composite electrodes, the charge-transfer mediators between the electrode and electrolyte are the graphitic particles. Enache *et al.* have reported



that the decay in the stability of the electrode material is due to the corrosion of the  $sp^2$  graphitic active species.<sup>[62]</sup>

To explore the potential application of NBUNCD/Si<sub>P</sub> in developing a compact energy storage device, a symmetric pouch cell was fabricated using NBUNCD/Si<sub>P</sub> as the primary electrode material, with 3M KOH serving as the electrolyte. A schematic illustration of the pouch cell is provided in the inset of Figure 11a. The CV profiles of the supercapacitor at varying scan rates, ranging from 20 to 100 mV s<sup>-1</sup>, within a 0-1 V potential window, are depicted in Figure 11a. The correlation between specific capacitance and scan rates is presented in Figure S15. The GCD curve, exhibiting a nearly triangular shape, confirms the EDLC behavior of the pouch cell. The variation in current densities, ranging from 20 to 40 μA cm<sup>-2</sup>, is presented in Figure 11b, while the inset of Figure 11c displays how the specific capacitance changes with respect to the applied current density. At a current density of 20 μA cm<sup>-2</sup>, the specific capacitance was recorded as 0.23 mF cm<sup>-2</sup>. The pouch cell demonstrated remarkable cycling stability, maintaining 94.83% of its initial capacitance after 1,000 charge-discharge cycles. A detailed comparison of the electrochemical performance parameters of the fabricated pouch cell with those of other reported nanostructured electrodes is provided in Table 3.<sup>[61-66]</sup> Additionally, the NBUNCD/Si<sub>P</sub> sample, with dimensions of 1×1 cm<sup>2</sup>, exhibited a maximum energy density of 31.98 μWh cm<sup>-2</sup> and a power density of 10 μW cm<sup>-2</sup>. Notably, while the comparison table reveals deficiencies in stability and/or capacity for other nanostructured electrodes, attributed to background or side reactions occurring at the electrode surface, the chemically inert nature of diamond in the NBUNCD/Si<sub>P</sub> composite ensures robust performance, further emphasizing its suitability for the EC-SC applications.<sup>[55]</sup>

Higher stability and enhanced EC performance are prominently observed for NBUNCD/Si<sub>P</sub>. This enhancement is primarily attributed to the substrate structuring, which facilitates the formation of micro-pyramids and the RIE process, consequently, the formation

of the nanorods. These structural modifications not only augment the aspect ratio of the material but also significantly increase the  $sp^2$ -graphitic carbon content within the sample. Moreover, the superior high energy density and power density resulting from the substantial specific capacitance establish its suitability for applications demanding high-performance energy storage. Overall, the synergistic effects of structural modifications and material properties position NBUNCD/Si<sub>P</sub> in high-performance EC-SC electrodes, promising advancements in energy storage technology.

### 3. CONCLUSIONS

This study highlights the superior EC-SC performance of NBUNCD/Si<sub>P</sub>. The NBUNCD/Si<sub>P</sub> electrode exhibits remarkable enhancement in energy density with 54.06  $\mu\text{Wh cm}^{-2}$  at a power density of 0.25  $\mu\text{W cm}^{-2}$ . In contrast, for the thin film samples, BUNCD/Si (planar morphology) and BUNCD/Si<sub>P</sub> (pyramidal morphology) exhibited lower energy densities of 15.32  $\mu\text{Wh cm}^{-2}$  and 14.80  $\mu\text{Wh cm}^{-2}$ , respectively, at the same power density of 0.25  $\mu\text{W cm}^{-2}$ . Furthermore, NBUNCD/Si<sub>P</sub> exhibits an impressive 95.5% retention of specific capacitance retention over 5000 cycles with 95% Coulombic efficiency. Comprehensive material characterization of NBUNCD/Si<sub>P</sub> shows that the sample possesses a higher content of  $sp^2$ -graphitic carbon and oxygen functional groups, contributing to enhanced electric double-layer capacitor behavior. Moreover, the surface area of NBUNCD/Si<sub>P</sub> is enhanced by the RIE nanostructures formed on the micro-pyramidal structures. As a result, efficient pseudocapacitance properties (specific capacitance of 53.7  $\text{mF cm}^{-2}$  at a current density of 2.54  $\text{mA cm}^{-2}$ ) and stability (94.04% after 5000 cycles) are observed for the sample. These findings underline the potential of NBUNCD/Si<sub>P</sub> as a promising electrode material for next-generation EC-SC, offering valuable guidance for future research and development in this field.

### 4. EXPERIMENTAL METHODS

*Fabrication of Si micro-pyramids:* Figure 1 shows a schematic representation of the fabrication of NBUNCD on Si<sub>p</sub>. The Si substrate was structured using the alkali etching technique to engineer the Si<sub>p</sub>. Firstly, (100) Si substrates (Figure 1a) were cleaned in acetone, isopropyl alcohol and demineralized water and then rinsed in a solution of KOH, isopropyl alcohol, and demineralized water (1:6:55) at 90°C for 45 minutes. This process resulted in the formation of micro-pyramidal structures over the Si substrate (Figure 1b). The structures were formed due to the preferential anisotropic etching along Si crystal planes.<sup>[70,71]</sup>

*Preparation of BUNCD films:* The BUNCD films were fabricated on Si<sub>p</sub> substrates using the linear antenna microwave plasma enhanced chemical vapor deposition (LA MW CVD) reactor (SCIA cube 300). First, the substrates were subjected to ultrasonic nucleation in a suspension of nanodiamond powder with a particle size of approximately 5 nm in deionized water. Trimethyl borate (TMBT) was employed as a carbon, boron, and oxygen source for film growth.<sup>[72]</sup> The 30-h growth was conducted in a gas mixture of H<sub>2</sub>, TMBT, CO<sub>2</sub> with a CO<sub>2</sub> to H<sub>2</sub> ratio of 0.2%. The flow rate of evaporated TMBT was maintained at 4% resulting in a B/C ratio of 328 000 ppm. The substrate temperature was maintained at 600 °C, and the pressure was kept at 30 Pa for forming BUNCD films on Si<sub>p</sub> substrates, designated as BUNCD/Si<sub>p</sub> (Figure 1c). For comparison, the BUNCD films were also grown on planar Si substrates, designated as BUNCD/Si.

*Fabrication of NBUNCD on Si micro-pyramids:* First, an 8 nm layer of Au was evaporated over the BUNCD/Si<sub>p</sub> film. The Au-coated BUNCD/Si<sub>p</sub> film underwent heat treatment in an H<sub>2</sub>-based microwave plasma for 10 min at 500 °C. This step resulted in the formation of self-organized nano-droplets of Au, arranged in an array over the surface of BUNCD/Si<sub>p</sub> (Figure 1d). The Au-masked diamond films underwent an etching process using a standard capacitively coupled plasma system (Phantom III, Trion Technology) with a mixture of oxygen and 5 % tetrafluoromethane (O<sub>2</sub>/CF<sub>4</sub> – 60/3 sccm) to fabricate one-dimensional nanorods on BUNCD

films. The pressure of 150 mTorr and the RF power of 150 W was maintained throughout the experiments. The etching process was carried out for 6 min. Following the RIE process, the remaining Au nano-droplets were removed by a standard wet chemical etching process ( $\text{HNO}_3\text{:HCl}$  at 1:3 n/n). The obtained samples were designated as NBUNCD/SiP (Figure 1e).

*Materials characteristics:* The morphological analysis of the BUNCD films was examined through field emission scanning electron microscopy (FESEM, Tescan MAIA3). Bruker D8 ADVANCE diffractometer with x-ray tube with Cu anode operating at 1.6 kW (40 kV/40 mA) were used for analyses of BUNCD layers. All x-ray measurements were performed in parallel beam geometry with a parabolic Goebel mirror in the primary beam. The x-ray diffraction (XRD) patterns were measured in grazing incidence set-up. Measurements were performed for the value of incidence angle  $\alpha = 0.3^\circ$ , in the angular range  $10^\circ\text{--}100^\circ$  with step size  $0.025^\circ$ . Parallel plate collimator with angular acceptance  $0.2^\circ$  was inserted in the diffracted beam. The bonding characteristics of the samples were investigated using micro-Raman spectroscopy (Renishaw, with  $\lambda = 532$  nm) and X-ray photoelectron spectroscopy (XPS, Phoibos 150, Specs). AFM topography characterization was performed by an NTEGRA Prima system (NT-MDT) using BudgetSensors probes - Multi75E-G. Data processing and analysis was done by Gwyddion software.

*Performance of supercapacitors:* A portable PalmSens potentiostat/galvanostat, version 4, controlled by PStace 5 software, was utilized for the EC measurements of BUNCD films. All evaluations of the EC-SC performance of BUNCD samples as working electrodes were conducted employing a three-electrode configuration, consisting of a reference electrode: Ag/AgCl electrode (immersed in saturated 3M KCl) and a counter electrode: Pt wire. Two types of electrolytes were employed for the EC measurements: an inert aqueous electrolyte, sodium sulphate (1 M  $\text{Na}_2\text{SO}_4$ ) and a redox-active electrolyte, ferro/ferri cyanide ( $0.05$  M  $[\text{Fe}(\text{CN})_6]^{3-}$ / $^{4-}$  in 1 M  $\text{Na}_2\text{SO}_4$ ) in the same cell set-up to study the electrical double layer capacitance

(EDLC) and pseudo capacitance (PC) behavior of the NBUNCD/SiP, respectively. The GCD measurements were carried out using the multistep potentiometry mode within the specified voltage range obtained from the CV measurements. EIS was employed to investigate the charge-transfer kinetics of the electrode. A two-electrode symmetric supercapacitor was fabricated to evaluate the full-cell performance, utilizing two NBUNCD/SiP films as electrodes and a 0.35 mm thick Whatman filter paper as the separator. The device employed 3M KOH solution as the electrolyte. CV, GCD and a 1000-cycle stability test of NBUNCD/SiP were conducted. The specific capacitance, energy density, and power density of the symmetric cell were also calculated.

### Acknowledgements

The authors would like to thank the financial support of the mobility project no. OLP-128, CZ CSIR-23-05 and by the MEYS OP JAC project no. CZ.02.01.01/00/22\_008/0004596 (SenDiSo). A.K., D.K.S., and O.S. thank the GACR bilateral project no. 23-04322L M.M. and M.V. thank the Research and Development Support Agency (APVV-23-0367) and VEGA grant (1/0631/22).

### References:

1. P. Simon, Y. Gogotsi, *Nature Mater* **2008**, *7*, 845.
2. A. K. Shukla, S. Sampath, K. Vijayamohanan, *Current Science* **2000**, *79* 1656. ISSN 0011-3891.
3. B. K. Kim, S. Sy, A. Yu, J. Zhang, J. *Handbook of Clean Energy Systems* **2015**, 1–25 (John Wiley & Sons, Ltd, 2015).
4. J. Meng, H. Guo, C. Niu, Y. Zhao, L. Xu, Q. Li, L. Mai, *Joule* **2017**, *1*, 522.
5. S. Rajagopal, R. Pulapparambil Vallikkattil, M. Mohamed Ibrahim, D.G. Velez, *Condens Matter* **2022**, *7*, 6.
6. X. Wang, Y. Li, F. Lou, M. E. Melandsø Buan, E. Sheridan, D. Chen, *RSC Adv* **2017**, *7*, 23859.
7. Dai, L., Chang, D.W., Baek, J.-B. and Lu, W., *Small* **2012**, *8*, 1130.
8. Z. Yu, L. Tetard, L. Zhai, J. Thomas, *Energy Environ Sci* **2015**, *8*, 702.

9. S. Yu, N. Yang, M. Vogel, S. Mandal, O. Williams, S. Jiang, H. Schönherr, B. Yang, X. Jiang, *Adv Energy Mater* **2018**, *8*, 1702947.
10. C. Portet, G. Yushin, Y. Gogotsi, *Carbon* **2007**, *45*, 2511.
11. M. D. Stoller, S. Park, Y. Zhu, J. An, R. S. Ruoff, *Nano Lett.* **2008**, *8*, 3498.
12. T. Ohashi, J. Zhang, Y. Takasu, W. Sugimoto, *Electrochim. Acta*, **2011**, *56*, 5599.
13. D. Banerjee, K. J. Sankaran, S. Deshmukh, M. Ficek, C. Yeh, J. Ryl, I. Lin, R. Bogdanowicz, A. Kanjilal, K. Haenen, S. Sinha Roy, *Nanoscale*, **2020**, *12*, 10117.
14. D. J. Garrett, K. Ganesan, A. Stacey, K. Fox, H. Meffin, S. Praver, *J Neural Eng* **2012**, *9*, 016002.
15. C. Hébert, E. Scorsone, A. Bendali, R. Kiran, M. Cottance, H. A. Girard, J. Degardin, E. Dubus, G. Lissorgues, L. Rousseau, P. Mailley, S. Picaud, P. Bergonzo, *Faraday Discuss.* **2014**, *172*, 47.
16. L. M. Silva, M. dos Santos, M. R. Baldan, A. F. Beloto, N. G. Ferreira, *Mater Res* **2015**, *18*, 1407.
17. D. Villarreal, J. Sharma, M. J. Arellano-Jimenez, O. Auciello, E. de Obaldía, *Mater* **2022**, *15*, 6003.
18. J. A. Carlisle and O. Auciello, *Electrochem. Soc. Interface* **2003**, *12*, 28.
19. S. Handschuh-Wang, T. Wang, Y. Tang, *Small* **2021**, *17*, 2007529.
20. N. Yang, J. S. Foord, X. Jiang, *Carbon N Y* **2016**, *99*, 90.
21. K. Okano, K. Hoshina, S. Koizumi, J. Itoh, *IEEE Electron Device Letters* **1995**, *16*, 239.
22. S. Gao, J. Seo, S. Hong, J. Li, P. Feng, J. Y. Byun, Y. J. Jung, *J Mater Chem C Mater* **2023**, *11*, 5102.
23. F. J. Wendisch, M. Rey, N. Vogel, G. R. Bourret, *Chem Mater* **2020**, *32*, 9425.
24. T. Chang, S. Lou, H. Chen, C. Chen, C. Lee, N. Tai, I. Lin, *Nanoscale* **2013**, *5*, 7467.
25. B. R. Huang, H. C. Chen, S. Jou, I. N. Lin, *Vacuum* **2009**, *84*, 111.
26. Y. F. Tzeng, C. Y. Lee, H. T. Chiu, N. H. Tai, I. N. Lin, *Diam Relat Mater* **2008**, *17*, 1817.
27. L. A. Gautier, V. Le Borgne, S. Al Moussalami, M. A. El Khakani, *Nanoscale Res Lett* **2014**, *9*, 1.
28. P. H. Tsai, H. Y. Tsai, *Thin Solid Films, Elsevier B.V.* **2015**, *584*, 330.
29. H. Li, S. Cheng, J. Li, J. Song, *J of Nanomater* **2015**, *2015*, 692562.
30. T. Kondo, K. Yajima, T. Kato, M. Okano, C. Terashima, T. Aikawa, M. Hayase, M. Yuasa, *Diam Relat Mater* **2017**, *72*, 13.
31. S. Szunerits, Y. Coffinier, E. Galopin, J. Brenner, R. Boukherroub, *Electrochem commun* **2010**, *12*, 438.
32. O. Auciello, A. V. Sumant, *Diam Relat Mater* **2010**, *19*, 699.

33. M. Salgado-Meza, G. Martínez-Rodríguez, P. Tirado-Cantú, E. E. Montijo-Valenzuela, R. García-Gutiérrez, *Appl Sci* **2021**, *11*, 8443.
34. J. Kurian, K. J. Sankaran, I. N. Lin, *Phys. Status Solidi A* **2014**, *211*, 2223.
35. O. Babchenko, A. Kromka, K. Hruska, M. Michalka, J. Potmesil, M. Vanecek, *Open Phys* **2009**, *7*, 310.
36. S. Kunuku, K. J. Sankaran, C. Y. Tsai, W. H. Chang, N. H. Tai, K. C. Leou, I. N. Lin, *ACS Appl Mater Interfaces* **2013**, *5*, 7439.
37. H. Uetsuka, T. Yamada, S. Shikata, *Diam Relat Mater* **2008**, *17*, 728.
38. M. L. Terranova, S. Orlanducci, A. Fiori, E. Tamburri, M. Rossi, V. Sessa, A. S. Barnard, *Chem Mater* **2005**, *17*, 3214.
39. Y. Zheng, J. Liu, R. Zhang, A. Cumont, J. Wang, J. Wei, C. Li, H. Ye, *J Mater Res* **2020**, *35*, 462.
40. S. Suman, D. K. Sharma, O. Szabo, B. Rakesh, M. Marton, M. Vojs, A. Vincze, S. P. Dutta, U. Balaji, D. Debasish, R. Sakthivel, K. J. Sankaran, A. Kromka, *J Mater Chem A* **2024**, *12*, 21134.
41. T. S. Le, M. Cretin, P. Huguet, P. Sistat, F. Pichot, *Nanosci* **2014**, *3*, 1.
42. D. Shi, L. Liu, Z. Zhai, B. Chen, Z. Lu, C. Zhang, Z. Yuan, M. Zhou, B. Yang, N. Huang, X. Jiang, *Journal of Materials Science & Technology* **2021**, *86*, 1-10.
43. D. Shi, N. Huang, L. Liu, B. Yang, Z. Zhai, Y. Wang, Z. Yuan, H. Li, Z. Gai, X. Jiang, *Appl. Surf. Sci.* **2020** *512*, 145652.
44. S. Suman, D. K. Sharma, S. Sain, O. Szabo, S. K. Sethy, B. Rakesh, U. Balaji, M. Marton, M. Vojs, S. S. Roy, R. Sakthivel, K. J. Sankaran, A. Kromka, *ACS Appl Electron Mater* **2023**, *5*, 4946.
45. V. Mortet, A. Taylor, Z. Vlčková Živcová, D. Machon, O. Frank, P. Hubík, D. Tremouilles, L. Kavan, *Diam Relat Mater* **2018**, *88*, 163.
46. V. Mortet, Z. Vlčková Živcová, A. Taylor, M. Davydová, O. Frank, P. Hubík, J. Lorincik, M. Aleshin, *Diam Relat Mater* **2019**, *93*, 54.
47. P. Szirmai, T. Pichler, O. A. Williams, S. Mandal, C. Bäuerle, F. Simon, *Phys. Status Solidi B* **2012**, *249*, 2656.
48. M. Bernard, A. Deneuve, P. Muret, *Diam Relat Mater* **2004**, *13*, 282.
49. R. Hoffmann, A. Kriele, H. Obloh, J. Hees, M. Wolfer, W. Smirnov, N. Yang, C. E. Nebel, *Appl Phys Lett* **2010**, *97*, 052103.
50. S. Ghodbane, D. Ballutaud, A. Deneuve, C. Baron, *Phys Status Solidi (a)* **2006**, *203*, 3147.
51. K. J. Sankaran, M. Ficek, K. Panda, C. J. Yeh, M. Sawczak, J. Ryl, K. C. Leou, J. Y. Park, I. N. Lin, R. Bogdanowicz, K. Haenen, *ACS Appl Mater Interfaces* **2019**, *11*, 48612–48623.
52. D. Vorselen, E. S. Kooreman, G. J. L. Wuite1, W. H. Roos, *Sci Rep* **2016**, *6*, 36972.

53. C. Xiao, F. Elam, S. van Vliet, R. Bliem, S. Lépinay, N. Shahidzadeh, B. Weber, S. Franklin, *Carbon N Y* **2022**, *200*, 1.
54. J. Wang, J. Tu, H. Lei, H. Zhu, *RSC Adv* **2019**, *9*, 38990.
55. F. Gao, C. E. Nebel, *ACS Appl Mater Interfaces* **2016**, *8*, 28244.
56. J. L. Qi, X. Wang, J. H. Lin, F. Zhang, J. C. Feng, W. D Fei, *J Mater Chem A Mater* **2015**, *3*, 12396.
57. J. B. Jorcin, M. E. Orazem, N. Pébère, B. Tribollet, *Electrochim Acta* **2006**, *51*, 1473.
58. Y. Zhou, J. Zhi, Y. Zou, W. Zhang, S. T. Lee, *Anal Chem* **2008**, *80*, 4141.
59. X. Li, J. Rong, B. Wei, *ACS Nano* **2010**, *4*, 6039–6049.
60. D. Banerjee, K. J. Sankaran, S. Deshmukh, C-J. Yeh, M. Gupta, I-N. Lin, K. Haenen, A. Kanjilal, S. S. Roy, *Electrochim Acta* **2021**, *397*, 139267.
61. D. Banerjee, K. J. Sankaran, S. Deshmukh, M. Ficek, C-J Yeh, j. Ryl, I-N Lin, R. Bogdanowicz, A. Kanjilal, K. Haenen, S. S. Roy, *Nanoscale* **2020**, *12*, 10117.
62. T. A. Enache, A. M. Chiorcea-Paquim, O. Fatibello-Filho, A. M. Oliveira-Brett, *Electrochem commun* **2009**, *11*, 1342.
63. I. Duo, A. Fujishima, C. Comninellis, *Electrochem commun* **2003**, *5*, 695.
64. M. Panizza, G. Siné, I. Duo, L. Ouattara, C. Comninellis, *Electrochem Solid-State Lett* **2003**, *6*, D17.
65. F. L. Souza, C. Saéz, M. R. V. Lanza, P. Cañizares, M. A. Rodrigo, *Electrochim Acta* **2016**, *187*, 119.
66. E. Eustache, C. Douard, A. Demortière, V. De Andrade, M. Brachet, J. Le Bideau, T. Brousse, C. Lethien, *Adv Mater Technol* **2017**, *2*, 1700126.
67. L. Kou, T. Huang, B. Zheng, Y. Han, X. Zhao, K. Gopalsamy, H. Sun, C. Gao, *Nat Commun* **2014**, *5*, 3754.
68. D. Banerjee, K. J. Sankaran, S. Deshmukh, M. Ficek, C. Yeh, J. Ryl, I. Lin, R. Bogdanowicz, A. Kanjilal, K. Haenen, S. Sinha Roy, *Nanoscale*, **2020**, *12*, 10117.
69. A. Mamoon, S. A. Zahra, Z. Khan, M. Ahmed, F. Nasir, M. Iqbal, M. A. Mohammad, A. Mahmood, D. Akinwande, S. Rizwan, *Front Mater* **2020**, *7*.
70. A. S. González, J. García, V. Vega, R. Caballero Flores, V. M. Prida, *ACS Omega* **2023**, *8*, 40087.
71. E. Scorsone, N. Gattout, L. Rousseau, G. B. Lissorgues. *Diam Relat Mater*, **2017**, *76*, 31.
72. P. Pal, V. Swarnalatha, A. V. N. Rao, A. K. Pandey, H. Tanaka, K. Sato, *Micro nano syst lett* **2021**, *9*, 4.
73. I. A. Shah, W. J. P. Van Enckevort, E. Vlieg, *Sens Actuators A Phys* **2010**, *164*, 154.
74. M. Marton, M. Vojs, P. Michniak, M. Behúl, V. Rehacek, M. Pifko, Š. Stehlík, A. Kromka, *Diam Relat Mater* **2022**, *126*, 109111.



**Table 1.** The equivalent circuit parameters values of BUNCD electrodes in 1M Na<sub>2</sub>SO<sub>4</sub> electrolyte.

<b>Element</b>	<b>BUNCD/Si</b>	<b>BUNCD/Si<sub>P</sub></b>	<b>NBUNCD/Si<sub>P</sub></b>	<b>Unit</b>
<b>R<sub>s</sub></b>	85.8	91.1	66.2	$\Omega$
<b>CPE</b>	6.9	15.1	19	$\mu\text{T}$
<b>n</b>	0.483	0.687	0.742	$\phi$
<b>R<sub>ct</sub></b>	0	622	591	$\Omega$
<b>C<sub>DL</sub></b>	1.1	3.4	18.1	$\mu\text{F}$

**Table 2.** The equivalent circuit parameter values of BUNCD electrodes in 0.05M  $[\text{Fe}(\text{CN})_6]^{3-}$  / $^{4-}$  in 1M  $\text{Na}_2\text{SO}_4$  electrolyte.

<b>BUNCD/Si</b>						
<b><math>R_s</math> (<math>\Omega</math>)</b>	<b><math>R_{CT}</math> (<math>\Omega</math>)</b>		<b><math>W_1</math> (<math>\sigma</math>)</b>		<b><math>C_{DL}</math> (<math>\mu\text{F}</math>)</b>	
89.1	0.37		12		425	
<b>BUNCD/Si<sub>p</sub></b>						
<b><math>R_s</math> (<math>\Omega</math>)</b>	<b><math>R_{CT}</math> (<math>\Omega</math>)</b>	<b><math>W_1</math> (<math>\sigma</math>)</b>		<b><math>CPE</math> (<math>\mu\text{T}</math>)</b>	<b><math>n_1</math> (<math>\phi</math>)</b>	
61.3	24.2	13.2		140.3	0.638	
<b>NBUNCD/Si<sub>p</sub></b>						
<b><math>R_s</math> (<math>\Omega</math>)</b>	<b><math>R</math> (<math>\Omega</math>)</b>	<b><math>CPE</math> (<math>\mu\text{T}</math>)</b>	<b><math>n_1</math> (<math>\phi</math>)</b>	<b><math>R_{CT}</math> (<math>\Omega</math>)</b>	<b><math>W_1</math> (<math>\sigma</math>)</b>	<b><math>C_{DL}</math> (<math>\mu\text{F}</math>)</b>
75.9	20.8	244	0.549	3.3	14.9	1460

**Table 3.** Comparison of EC-SC parameters of NBUNCD/Si<sub>P</sub> with other reported nanostructured electrodes.

Sample	Electrolyte	Stability (number of cycles)	Sp. capacitance (current density)	Energy density	Power density	Reference
3D symmetric MnO <sub>2</sub> /MnO <sub>2</sub> MSCs	0.05 M Na <sub>2</sub> SO <sub>4</sub> EMI TFSI	>80% (15000) 80% (6000)	113 mF/cm <sup>2</sup> @ 1 mA/cm <sup>2</sup> 20 mF/cm <sup>2</sup> @0.4 mA/cm <sup>2</sup>	10 μWh/cm <sup>2</sup> 6.5 μWh/cm <sup>2</sup>	20 mW/cm <sup>2</sup> 8 mW/cm <sup>2</sup>	[61]
RGO+CNT@CMC	PVA/H <sub>3</sub> PO <sub>4</sub>	~100% (2000)	177 mF/cm <sup>2</sup> @ 0.1 mA/cm <sup>2</sup>	3.84 μWh/cm <sup>2</sup>	20 μW/cm <sup>2</sup>	[62]
hybrid carbon nanograss	0.05 M [Fe(CN) <sub>6</sub> ] <sup>3-/4-</sup> in 1M Na <sub>2</sub> SO <sub>4</sub>	95% (10000)	0.25F/cm <sup>2</sup> @ 3 mA/cm <sup>2</sup>	78.1-17.7 μWh/cm <sup>2</sup>	2.8-18.7 mW/cm <sup>2</sup>	[63]
LRPI	PVA-KOH	-	2.19 mF/cm <sup>2</sup> (@20 mV/s)	1.21 μWh/cm <sup>2</sup>	21.9 μW/cm <sup>2</sup>	[64]
3D-NSE	5 M KOH	95% (2600)	500 mF/cm <sup>2</sup> (@6.4 mA/cm <sup>2</sup> )	385.87 μWh/cm <sup>2</sup>	3.82 μW/cm <sup>2</sup>	[65]
BDD/PPY	0.5 M H <sub>2</sub> SO <sub>4</sub> 0.5 M TEABF <sub>4</sub> (PC)	- -	1.31 mF/cm <sup>2</sup> (@10 mV/s) 0.42 mF/cm <sup>2</sup> (@10 mV/s)	1 μWh/cm <sup>2</sup> 0.17 μWh/cm <sup>2</sup>	700 μW/cm <sup>2</sup> 200 μW/cm <sup>2</sup>	[66]
NBUNCD/Si <sub>P</sub>	3 M KOH	94.8% (1000)	0.23 mF/cm <sup>2</sup> (@20 μA/cm <sup>2</sup> )	31.98 μWh/cm <sup>2</sup>	10 μW/cm <sup>2</sup>	This work**

## Figure captions

**Figure 1.** Schematic representation of the fabrication of nanostructured BUNCD on Si micro-pyramids.

**Figure 2.** FESEM micrographs (a) micro-pyramidal Si substrate, (b) BUNCD/Si<sub>P</sub>, and (c) NBUNCD/Si<sub>P</sub> with (a<sub>I</sub>, b<sub>I</sub>, c<sub>I</sub>) 45° angle view, (a<sub>II</sub>, b<sub>II</sub>, c<sub>II</sub>) plan-view, and (a<sub>III</sub>, b<sub>III</sub>, c<sub>III</sub>) cross-sectional view.

**Figure 3.** Schematic representation of the mechanism of nanostructure fabrication on BUNCD films using RIE.

**Figure 4.** (a) Raman spectra and (b) XPS spectra of C1s and (c) XPS spectra O1s deconvoluted peaks of BUNCD samples for I. BUNCD/Si, II. BUNCD/Si<sub>P</sub>, and III. NBUNCD/Si<sub>P</sub>.

**Figure 5.** Cyclic voltammogram study in 1M Na<sub>2</sub>SO<sub>4</sub> at varied scan rates from 10-100 mV s<sup>-1</sup> of BUNCD samples, (a) BUNCD/Si, (b) BUNCD/Si<sub>P</sub>, (c) NBUNCD/Si<sub>P</sub>, and (d) a comparison of the current response of these BUNCD samples at 60 mV s<sup>-1</sup>.

**Figure 6.** Galvanostatic charging-discharging study with varying current densities in 1M Na<sub>2</sub>SO<sub>4</sub> of BUNCD samples, (a) BUNCD/Si, (b) BUNCD/Si<sub>P</sub>, (c) NBUNCD/Si<sub>P</sub>, and (d) a comparison of electrochemical impedance spectra of these BUNCD samples with the inset showing the equivalent circuit fitted to the EIS spectra for I. BUNCD/Si, II. BUNCD/Si<sub>P</sub>, and III. NBUNCD/Si<sub>P</sub>.

**Figure 7.** Cyclic voltammogram study in 0.05 M [Fe(CN)<sub>6</sub>]<sup>3-/4-</sup> contained in 1M Na<sub>2</sub>SO<sub>4</sub> at varied scan rates from 10-100 mV s<sup>-1</sup> of BUNCD samples, (a) BUNCD/Si, (b) BUNCD/Si<sub>P</sub>, (c) NBUNCD/Si<sub>P</sub>, and (d) a comparison of the current response of these BUNCD samples at 60 mV s<sup>-1</sup>.

**Figure 8.** Galvanostatic charging-discharging study with varying current densities in 0.05 M  $[\text{Fe}(\text{CN})_6]^{3-/4-}$  contained in 1M  $\text{Na}_2\text{SO}_4$  of BUNCD samples, (a) BUNCD/Si, (b) BUNCD/SiP, (c) NBUNCD/SiP.

**Figure 9.** Electrochemical Impedance Spectroscopy in 0.05M  $\text{Fe}(\text{CN})_6^{3-/4-}$  contained in 1M  $\text{Na}_2\text{SO}_4$  of BUNCD samples, (a) BUNCD/Si, (b) BUNCD/SiP, and (c) NBUNCD/SiP, with (a<sub>I</sub>, b<sub>I</sub>, c<sub>I</sub>) EIS spectra and (a<sub>II</sub>, b<sub>II</sub>, c<sub>II</sub>) corresponding equivalent circuit for the EIS spectra.

**Figure 10.** Retention of specific capacitance (a, b) and Coulombic efficiency (c, d) of the BUNCD samples calculated from 5000 cycles of charging-discharging in (a, c) 1M  $\text{Na}_2\text{SO}_4$  and (b, d) 0.05M  $[\text{Fe}(\text{CN})_6]^{3-/4-}$  contained in 1M  $\text{Na}_2\text{SO}_4$ , I. BUNCD/Si, II. BUNCD/SiP, and III. NBUNCD/SiP.

**Figure 11.** Schematic representation of the symmetric pouch cell with NBUNCD/SiP, shown in the inset of (a), along with (a) cyclic voltammetry, (b) galvanostatic charge-discharge curve, and (c) life cycle stability measurement (inset showing specific capacitance calculations from (b)) of the symmetric cell using NBUNCD/SiP in 3M KOH.

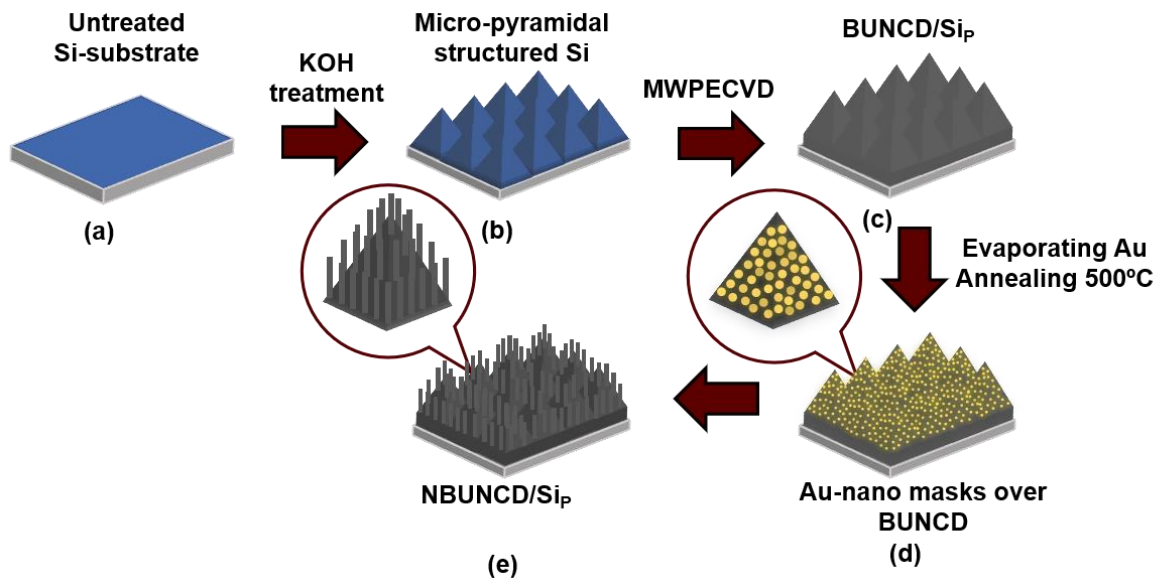


Figure 1.

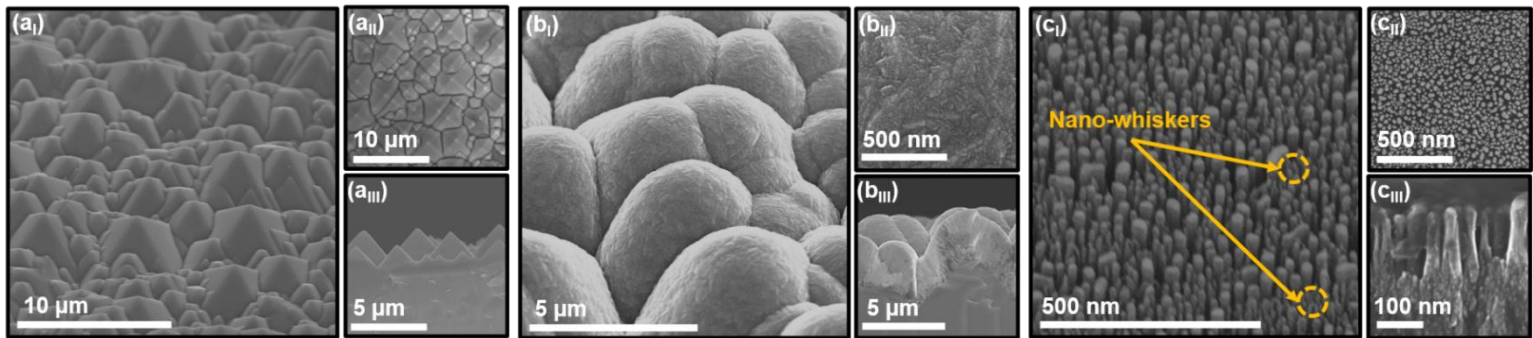


Figure 2.

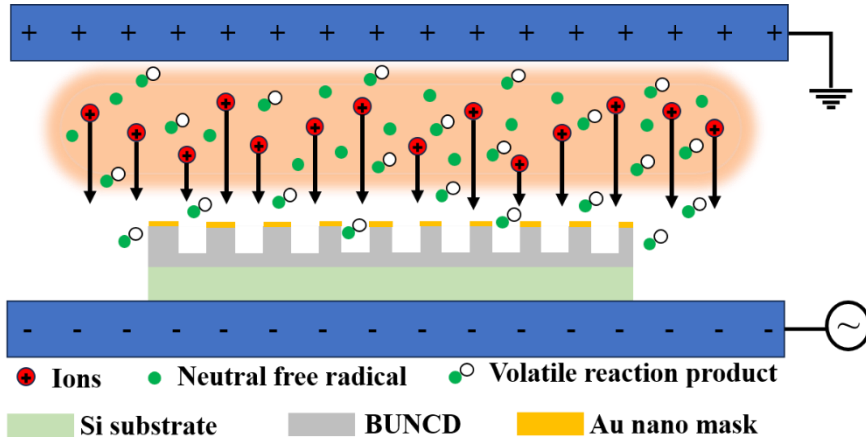


Figure 3.

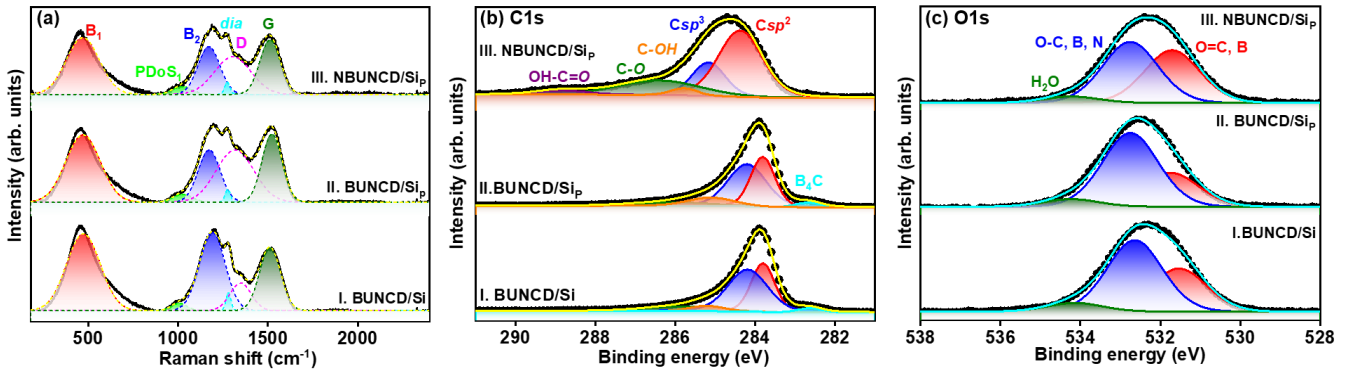


Figure 4.

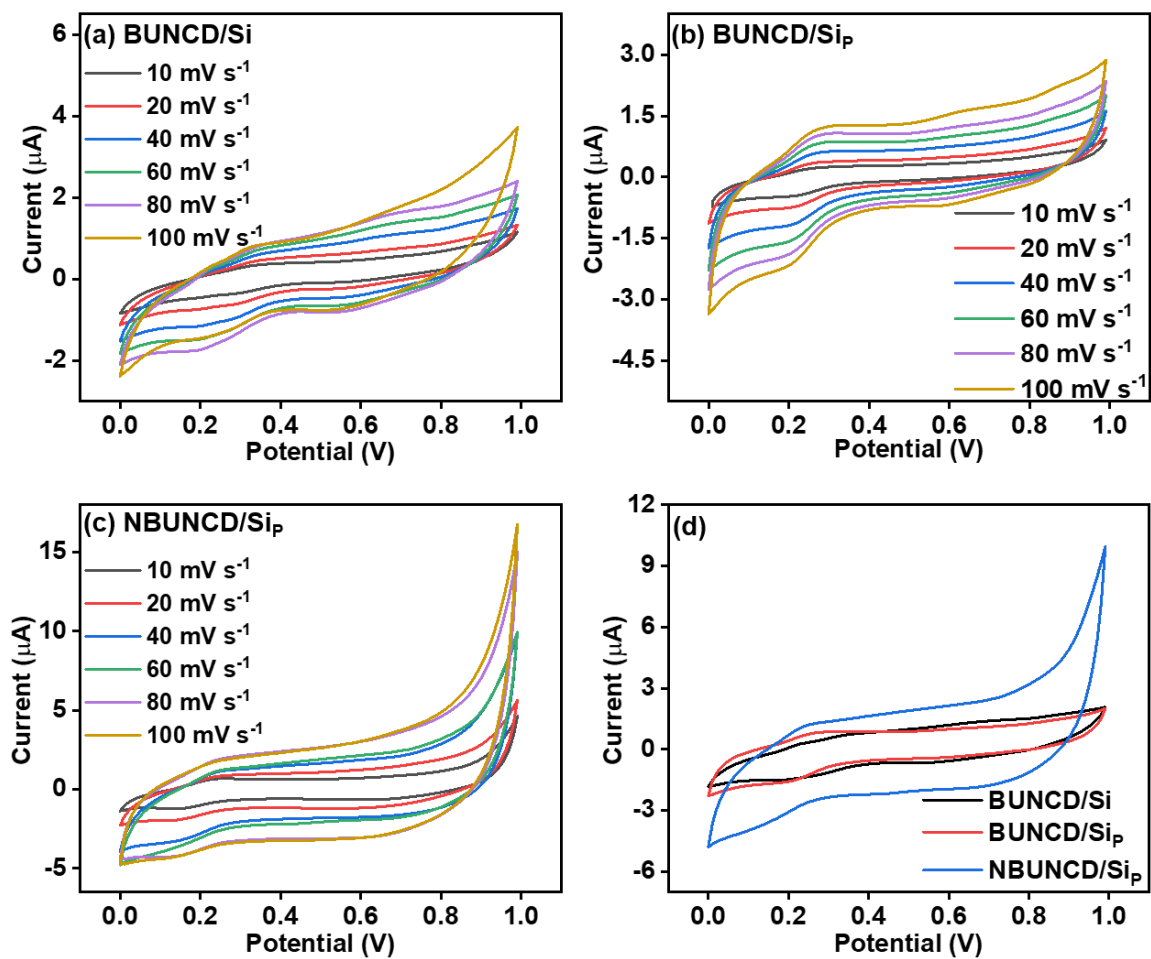


Figure 5.



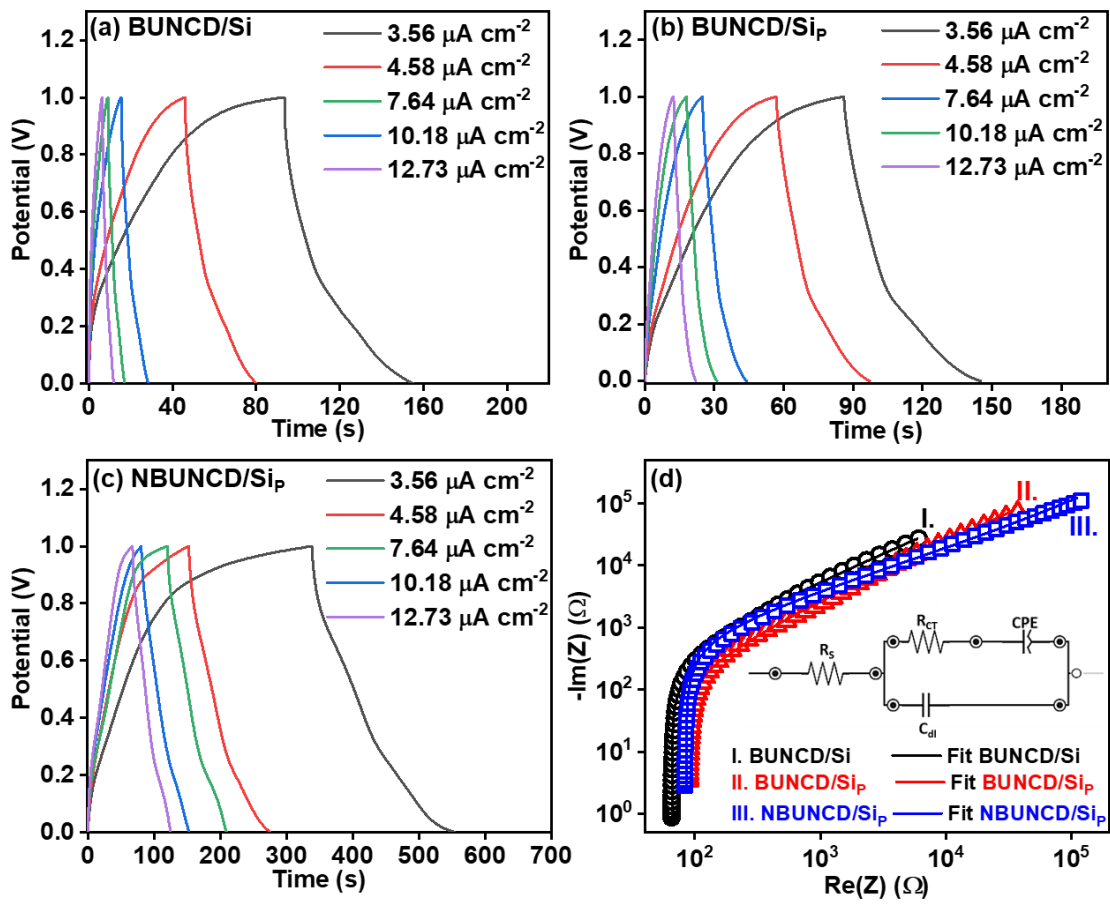


Figure 6.

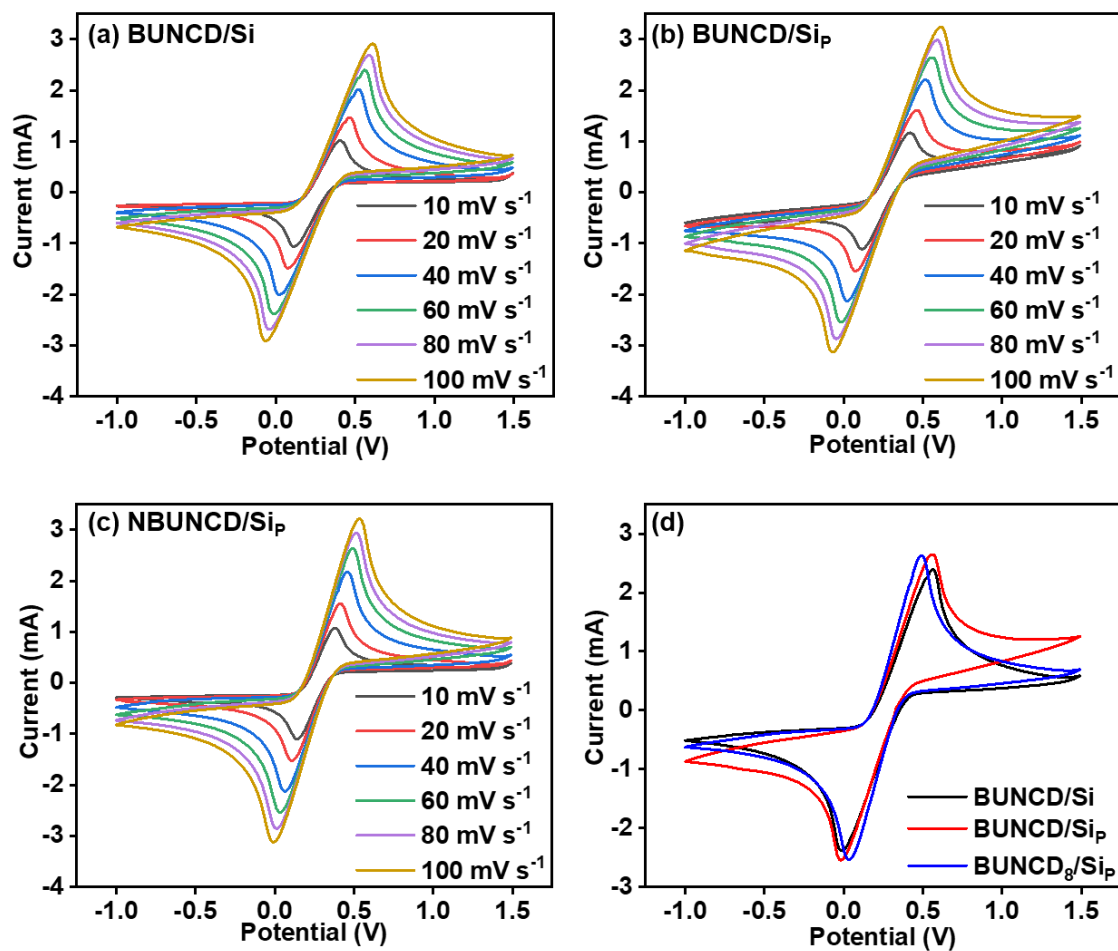


Figure 7.

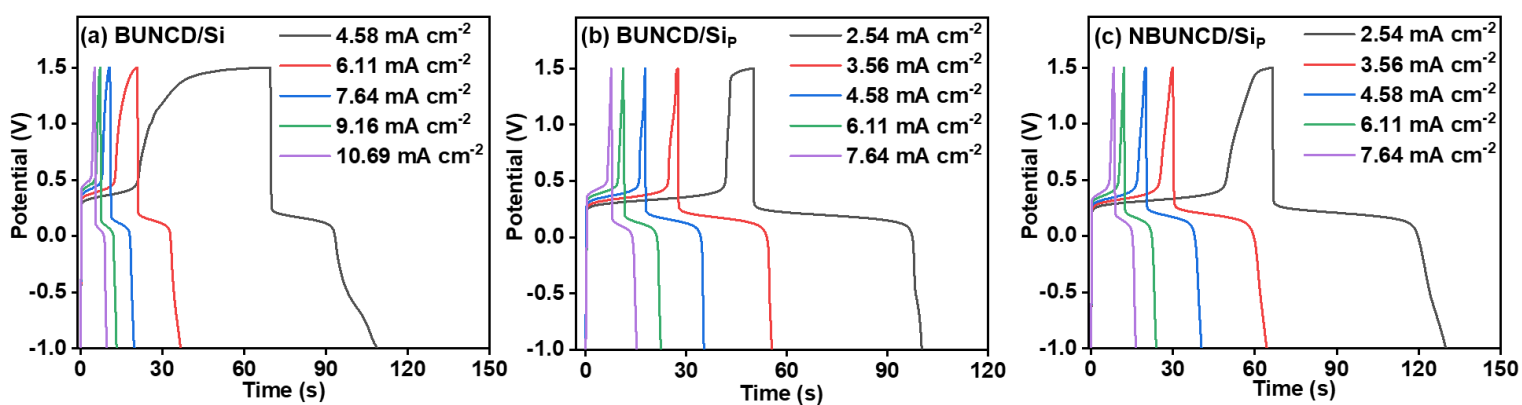


Figure 8.

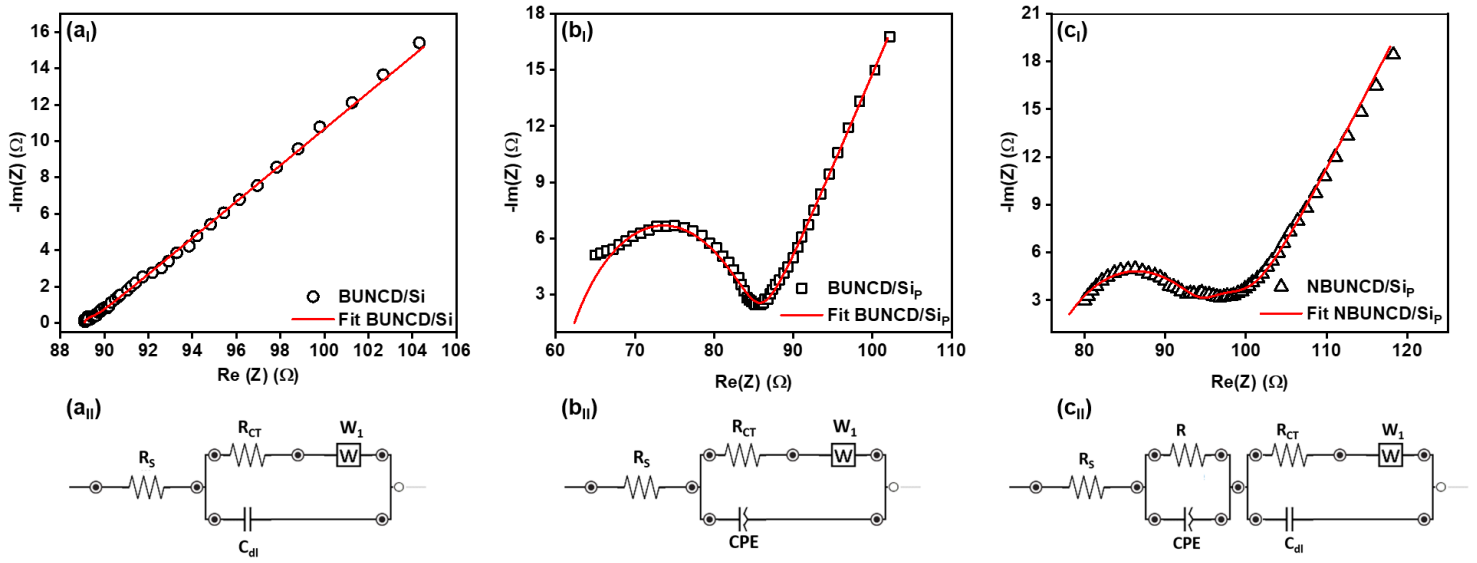


Figure 9.

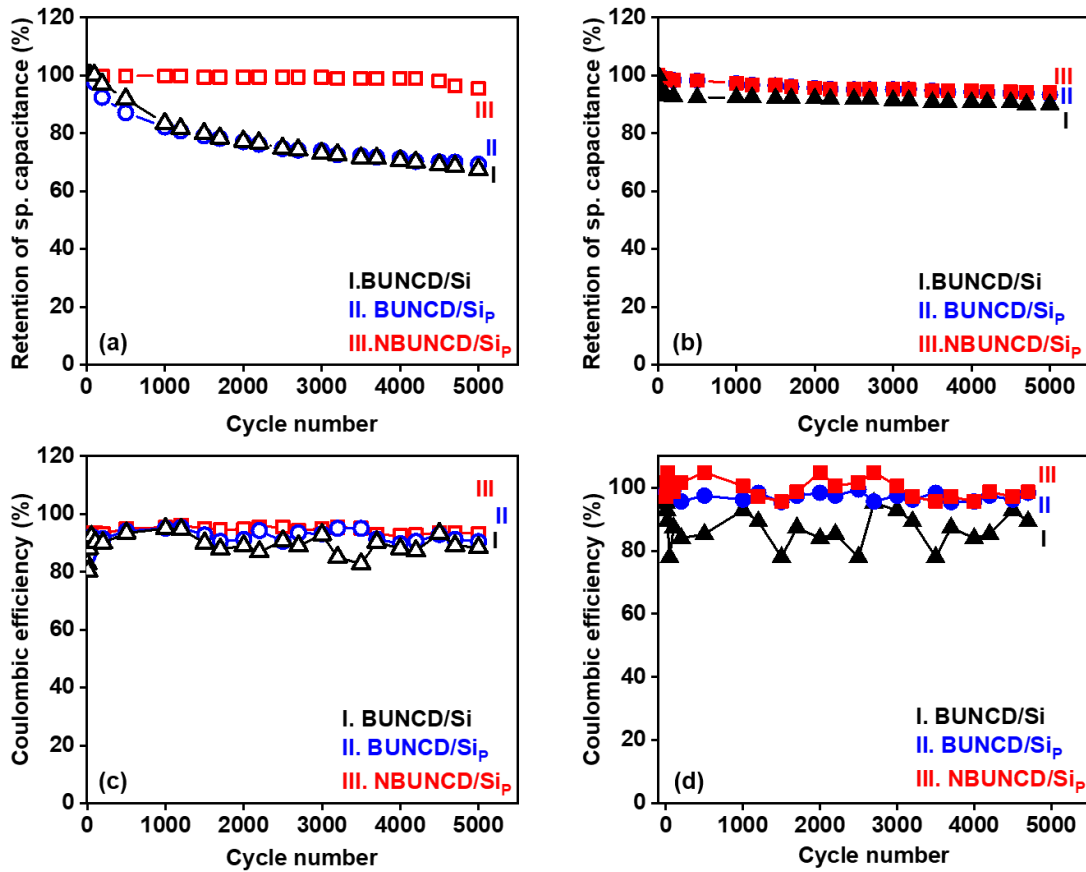


Figure 10.

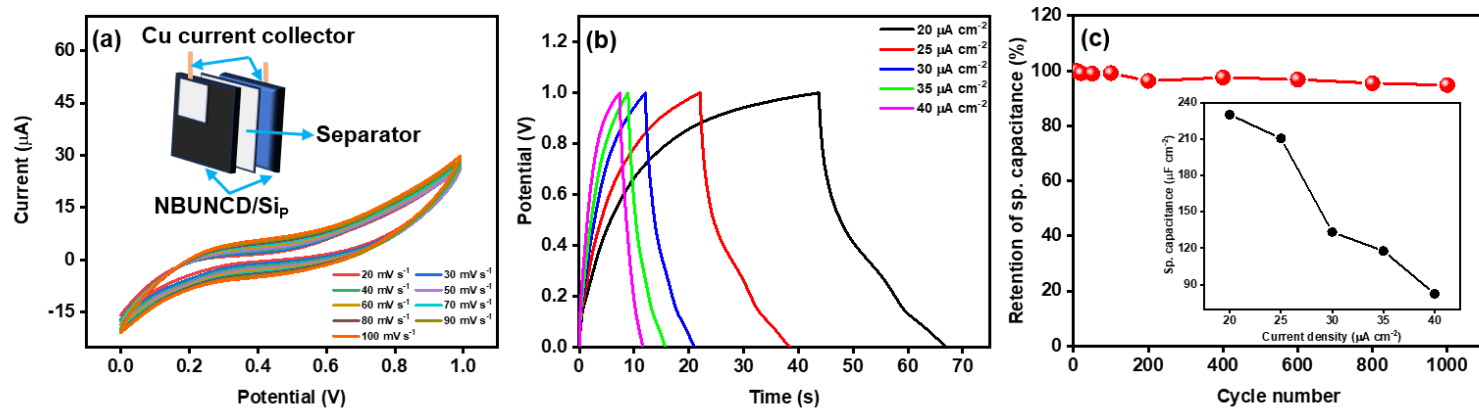


Figure 11.